21 cm Emission from Ionized Clouds of UV Sources in the Reionization Epoch

Long-Long Feng[1,2], Jing-Mei Qiu[3], Chi-Wang Shu[3], and Li-Zhi Fang[4]

ABSTRACT

We study the formation and evolution of hot ionized IGM surrounding point sources of UV photons in reionization epoch with numerical solutions of radiation transfer in phase space. We show that in the first stage the ionizing and heating fronts of IGM are coincident, and propagate with the speed of light. In later stage, when the frequency spectrum of UV photons is hardened, the propagation of both the ionizing and heating fronts is less than the speed of light, and the heating front is always beyond the ionizing front. In the spherical shell between the ionizing and heating fronts, the IGM is heated to $T \simeq 10^4$, while atoms are almost neural. Therefore, the shell is the region of 21 cm emission. The brightness temperature excess upon the CMB is about 20 mK. The scales (radius and thickness) of the 21 cm emission shell are approximately proportional to $\dot{E}^{1/3}$, $\dot{E}$ being the intensity of the source. For a source at redshift $z = 9$ with intensity $\dot{E} = 10^{45}$ ergs s^{-1} and power-law spectrum ν^{-2}, the 21 cm emission shell is in the radial (comoving) range from 4 to 10 h^{-1} Mpc. These 21 cm emission patches would be detectable with planned and ongoing projects of meter band radio instrumentation. Since in this problem the phase space solution of radiative transfer is essential, we also briefly present the algorithm based on the WENO code.

Subject headings: cosmology: theory - gravitation - hydrodynamics - methods: numerical - shock waves

---

[1]Purple Mountain Observatory, Nanjing, 210008, P.R. China.

[2]National Astronomical Observatories, Chinese Academy of Science, Chao-Yang District, Beijing 100012, P.R. China

[3]Division of Applied Mathematics, Brown University, Providence, RI 02912

[4]Department of Physics, University of Arizona, Tucson, AZ 85721

1. Introduction

Primordial hydrogen and helium of the universe, created at the time of nucleosynthesis, recombine with electrons to become neutral hydrogen and helium at redshift $z \sim 1000$. Before $z = 137$, the residual ionization of the cosmic gas keeps its temperature locked to the CMB temperature. After that the gas cools down adiabatically during the expansion of the universe. At $z = 20$, the temperature of the baryon gas is a few degree K. Reionization of the baryon gas may begin at the redshift range $30 > z > 10$ when the first generation stars form, and then UV photons are produced (e.g. Page et al 2006). In the first stage of reionization, the field of hydrogen gas has a patchy structure. That is, most space is still filled by neutral hydrogen in low temperature, but fully ionized patches with high temperature around isolated UV photon sources appear.

A possible way to study the ionized patches is to detect redshifted 21 cm line emission/absorption signatures against cosmic microwave background. The detectability of this signal has been estimated in various models of the IGM heating (Madau & Rees 2000, Tozzi et al. 2000, Cen & Haiman 2000, Wyithe & Loeb 2004). These works are based on the equilibrium condition or the rate equation of photons. They generally concluded that the 21 cm signal would be detectable with ongoing or planned projects of meter radio wave array, such as the 21 cm Array (21CMA) (e.g. Peterson, et al. 2005), Low Frequency Array (LOFAR) (e.g. Rottgering 2003) and Square Kilometer Array (SKA) (e.g. van de Weygaert & van Albada 1996). However, a challenge to identify the redshifted 21 cm signal from the recombination is the foreground contamination, including the noise from the artificial radio interference in the VHF band. Therefore, to identify the redshifted 21 cm emission of reionization, we should search for the features of the redshifted 21 cm emission, which can be used to distinguish the 21 cm emission of reionization from contamination. For instance, the non-Gaussianity of the field of brightness temperature excess, δT_b, of 21 cm emission reionization would be useful to draw information from the noisy observation (He et al. 2004).

Similarly, to identify the 21 cm emission from an isolated UV photon source at the early stage of reionization, we should calculate the profile of the 21 cm emission. For this purpose, the methods of the equilibrium condition and/or rate equation estimation are not enough, because in these approaches the distribution of neutral hydrogen fraction $f_{\rm HI}(r)$ generally is put by hand. For instance, it is assumed that the patchy structure can be described by the Stromgren sphere, i.e. fully ionized bubbles embedded in an HI background (Stromgren, 1939, Spitzer 1978; Osterbrock, 1989). However, the Stromgren sphere solution is reasonable only if the mean free path of photons, λ is much smaller than the Stromgren radius R_s. For strong sources, like quasars, the condition $\lambda \ll R_s$ would be true, but this may not be the case for weak sources, such as the first generation of stars. The time dependence of the

ionized radius $r \propto t^{1/3}$, given by these methods is actually unphysical. More importantly, the rate equation does not describe the evolution of the spectrum of UV photons, which is essential in studying the heating of baryon gas.

We will present a consistent calculation of the 21 cm emission profile using the radiative transfer equation. Recently, we have developed the WENO (Weighted Essentially Non-Oscillatory) algorithm on the cosmological hydrodynamical equations and radiative transfer equations (Feng et al. 2004; Qiu et al. 2006). It is effective to find the solutions describing the evolution of radiation in the phase space. With the WENO algorithm, in this paper, we will calculate the evolution of the profile of an ionized sphere and its 21 cm emission around a point UV source.

This paper is organized as follows. Section 2 presents the structures and evolution of ionization and temperature of baryon gas around a UV photon source. Section 3 gives the profile of 21 cm emission of this source. The discussion and conclusion are presented in Section 4. The equations used in the numerical calculation and the essential points of the WENO method are given in the Appendix.

2. Ionized Sphere

2.1. Basic Formulae

We consider the ionization of a uniformly distributed hydrogen gas with number density n by a point UV photon source located at $r = 0$. For simplicity we did not consider the component of helium of IGM, as it will not change the result essentially. If the expansion of the universe is ignored, the radiative transfer equation of the specific intensity $J(t, r, \nu)$ is (see the Appendix)

$$\frac{\partial J}{\partial (ct)} + \frac{1}{r^2}\frac{\partial}{\partial r}\left(r^2 J\right) = -k_\nu J + S \tag{1}$$

where ν is the frequency of photon. Supposing the source is at the center $r = 0$, instead of adding the source term S in the r.h.s of eq.(1), equivalently, we impose a boundary condition

$$\lim_{r\to 0} 4\pi r^2 J(t, r, \nu) = \dot{E}(\nu) \tag{2}$$

where $\dot{E}(\nu)d\nu$ is the energy of photons emitted from the central source per unit time within the frequency range from ν to $\nu + d\nu$. We assume $\dot{E}(\nu) = \dot{E}_0(\nu_0/\nu)^\alpha$, where α is the index of the power law. Therefore, integrating of $\dot{E}$ over ν gives the total intensity (energy per unit time) of ionizing photons emitted by the source, $\dot{E} = \int_{\nu_0}^{\infty} \dot{E}(\nu)d\nu = \dot{E}_0\nu_0/(\alpha - 1)$.

The absorption coefficient of eq.(1) is $k_\nu = \sigma(\nu) n_{\rm HI}(t, \mathbf{x})$, where the cross section $\sigma(\nu) = \sigma_0(\nu_0/\nu)^3$ and $\sigma_0 = 6.3\times10^{-18}$ cm^2, ν_0 is the ionization energy of the ground state of hydrogen $h\nu_0 = 13.6$ eV. The evolution of the number density of neutral hydrogen H I, $n_{\rm HI}(t, r)$, is governed by the ionization equation,

$$\frac{df_{\rm HI}}{dt} = \alpha_{\rm HII} n_e f_{\rm HII} - \Gamma_{\gamma\rm HI} f_{\rm HI} - \Gamma_{\rm eHI} n_e f_{\rm HI} \tag{3}$$

where the fraction of neutral hydrogen $f_{\rm HI} \equiv n_{\rm HI}(t, r)/n$ and n_e is the number density of electrons. In eq.(3), $\alpha_{\rm HII}$ is the recombination coefficient and $\Gamma_{\rm eHI}$ is the collision ionization rate. The photoionization rate $\Gamma_{\gamma\rm HI}(t, r)$ is given by

$$\Gamma_{\gamma\rm HI}(t, r) = \int_{\nu_0}^{\infty} d\nu \frac{J(t, r, \nu)}{h\nu} \sigma(\nu). \tag{4}$$

The kinetic temperature of baryon gas is determined by

$$k_B \frac{dT}{dt} = H - C \tag{5}$$

where k_B is the Boltzmann constant, and the temperature T is in unit of K. The details of the heating H and cooling C are given in the Appendix.

It is convenient to introduce the dimensionless variables of time, space and frequency defined by $t' = c\sigma_0 n t$, $r' = \sigma_0 n r$ and $nu' = \nu/\nu_0$. It means that t' and r' are respectively, the time and distance in units of mean free flight time and mean free path of photon $h\nu_0$ in neutral hydrogen gas with density n. In the ΛCDM model, $n = 1.88 \times 10^{-7}(1 + z_r)^3$ cm^{-3}, where z_r is the redshift of reionization, the unit of t' is $0.89 \times 10^6 (1 + z_r)^{-3}$ years, and the unit of r' is $0.27(1 + z_r)^{-3}$ Mpc. Correspondingly, the intensity is rescaled by $Jd\nu = (1/r^2)(h\nu_0/\sigma_0^3 n) J' d\nu'$. Thus, eqs.(1), (2), (4) and (5) become

$$\frac{\partial J'}{\partial t'} + \frac{\partial J'}{\partial r'} = -\left(\frac{1}{\nu'}\right)^3 f_{\rm HI} J', \tag{6}$$

and

$$c\sigma_0 \frac{df_{\rm HI}}{dt'} = \alpha_{\rm HII} f_{\rm HII}^2 - \frac{\Gamma_{\gamma\rm HI}}{n} f_{\rm HI} - \Gamma_{\rm eHI}(1 - f_{\rm HI}) f_{\rm HI}. \tag{7}$$

$$\frac{\Gamma_{\gamma\rm HI}(t, r)}{n} = \frac{1}{r'^2} \int_1^{\infty} d\nu' \frac{J'(t, r, \nu')}{\nu'} \frac{1}{\nu'^3} \tag{8}$$

$$c\sigma_0 k_B \frac{dT}{dt'} = H - C. \tag{9}$$

where we have assumed $n_e/n = f_{\rm HII}$ and $f_{\rm HII} = 1 - f_{\rm HI}$.

The point source condition eq.(2) requires $\dot{E}(\nu)d\nu = 4\pi(h\nu_0/n\sigma_0^3)J'(t,0,\nu')d\nu'$. If we take $J'(t,0,\nu') = J_0(1/\nu')^\alpha$, the total intensity of the source is given by

$$\dot{E} = \frac{4\pi h\nu_0}{(\alpha-1)n\sigma_0^3}J_0 = 5.8\times10^{42}\frac{1}{\alpha-1}\left(\frac{10}{1+z_r}\right)^3\left(\frac{J_0}{10^{-3}}\right) \quad \text{erg/s}. \tag{10}$$

2.2. Profiles of T and $f_{\rm HI}$

21 cm emission is from the region with high kinetic temperature and high fraction of neutral hydrogen H I. Therefore, we first calculate the profile of $T(t',r')$ and $f_{\rm HI}(t',r')$ around a point source. For simplicity, we use t, r, ν to stand for t', r' and ν' below. A typical result is plotted in Figure 1, for which the initial condition ($t=0$) is $T(r) = 10$ K, and $J'(r) = 0$. The top and bottom panels of Figure 1 show, respectively, the profiles of $T(r)$ and $f_{\rm HI}(r)$ at time $t = 1,000$ for sources $J_0 = 10^{-6}$, 10^{-4} and 10^{-2}, and 1, corresponding to $\dot{E} = 10^{39} - 10^{45}$ erg s^{-1} if $\alpha = 2$ at reionization redshift $1+z_r = 10$ (which roughly correspond to the emission rate of the number of ionizing photons $\dot{N} \simeq 10^{50} - 10^{56}$).

For sources of $J_0 > 10^{-6}$ the profile of $f_{\rm HI}(r)$ (bottom panel of Figure 1) can be approximated as a Stromgren sphere

$$f_{\rm HI}(r) = \begin{cases} 1 & r > R_s, \\ \ll 10^{-4} & r < R_s \end{cases} \tag{11}$$

where the ionized radius R_s depends on the intensity of source, J_0, and time t. Hydrogen is almost fully ionized within the sphere of radius R_s, while outside the sphere hydrogen atoms remain neutral. On the other hand, the profiles of T (top panel of Figure 1) have a tail. It goes down to low temperatures with r softly.

As indicated in Figure 1, an important feature for all sources with different intensities is that the heating occurs in larger regions than that of ionization. In the regions with $f_{\rm HI}(r) \simeq 1$, the tail of T has high temperature $T > 10^3$ K. It is due to the difference between hard and soft photons. Soft photon is effective to ionize IGM, while hard photon is more effective to heat IGM. In the region $r > R_s$, the IGM has already been significantly heated by hard photons, while the ionization rate is still not strong enough to build an ionized region. This point can also be seen from the fact that the high temperature tail is more significant for weak sources, because for the soft photons of weak sources are exhausted within a small range, and the ratio between hard and soft photons in the range $r > R_s$ is higher for weaker sources.

Figure 2 presents the time-dependence of the profiles of $T(t,r)$ and $f_{\rm HI}(t,r)$ for a source of $J_0 = 10^{-2}$, or $\dot{E} = 10^{43}$ ergs s^{-1}. It shows again that the heating ranges $T > 10^3$ K are

always larger than ionized ranges. The difference between the heating and ionizing sizes is larger for later time. This is because the ratios between hard and soft photons are larger at later time. In other words, a strong source will be similar to a weak source at large distance r from the source.

Figure 3 shows the evolution of $r_{90}(t)$, which is defined by $f_{\rm HI}(t, r_{90}) = 0.90$. It denotes the size, within which, i.e. $r < r_{90}$, 90% hydrogen are ionized. For a strong source, such as $J_0 = 1$, or $\dot{E} = 10^{45}$ ergs s^{-1}, we have approximately $r_{90} = t$, which implies that the ionizing region grows with an ionizing front propagating in the speed of light. But for weak sources, the growth of the ionizing region is much less than that of $r = t$. For weak sources their $r_{90}(t)$ are also following t at very small t, but become $r_{90}(t) < t$ when t is large. The weaker the sources, the earlier the stage of $r_{90}(t) < t$ takes place. One can define a time t_i or $r_{90}(t_i)$, larger than which, r_{90} will be less than t. The numbers of $r_{90}(t_i)$ and t_i characterize, respectively, the spatial scale of the ionizing sphere and the time scale to form such a sphere. At time $t > t_i$, the ionizing sphere is still increasing, but very slowly. In all cases, the time-dependence of $r_{90}(t)$ can not be approximated as $r_{90}(t) \propto t^{1/3}$ (e.g. Cen & Haiman 2000; Yu & Lu 2005). At very small t, $r_{90}(t) \propto t$, while at large t, the growth of $r_{90}(t)$ is much slower than $t^{1/3}$.

2.3. Spectral Evolution

As mentioned above, the difference of the evolution of hard and soft photons are crucial in the formation of the region of high T and high $f_{\rm HI}$. This point can be seen with the evolution of the frequency spectrum of photons.

The top panel of Figure 4 gives the frequency spectra of 1.) source $J_0 = 10^{-2}$ at time $t = 1,000$ and positions $r = 300$, 400 and 500, and 2.) source $J_0 = 1$ at time $t = 1,000$ and positions $r = 700$ and 900. We can see a significant r-dependence of the frequency spectrum. At a small r (300 for $J_0 = 10^{-2}$ and 700 for $J_0 = 1$) the spectra are still the original power-law spectrum $\nu^{-\alpha}$ with $\alpha = 2$, while at $r = 400$ for $J_0 = 10^{-2}$ and 900 for $J_0 = 1$, they are significantly hardened. It shows a peak at $\nu > 1$, similar to a spectrum of self-absorption. At high frequency $\nu > 50$, the spectra are still of power-law with $\alpha = 2$, while spectra at $\nu < 50$ are substantially dropped. Generally, self-absorption makes the lack of photons with $\nu \simeq 1$, and consequently leads to the spectral hardening of photons. The hardened spectrum would be effective for heating, but not for ionization.

The spectral hardening can be measured by the index of power law defined as

$$\alpha = -\frac{\partial \ln J}{\partial \ln \nu}. \tag{12}$$

Figure 5 plots α vs. ν for the frequency spectra of Figures 4. Obviously, α becomes smaller at larger r.

3. 21 cm Emission

3.1. 21 cm Emission

The 21 cm ($\nu_0 = 1420$ MHz) line emission associated with the spin-flip transition in neutral hydrogen (HI) at redshift z is determined by the spin temperature T_s. There are two mechanisms leading to $T_s(z) > T_{\rm CMB}(z) = 2.73(1+z)$ K, collision and radiation background, which gives (Field 1958, 1959)

$$T_s = \frac{T_{\rm CMB} + y_c T + y_{\rm L} T_{\rm L}}{1 + y_c + y_{\rm L}}. \tag{13}$$

In the patch phase of recombination, the photoionization UV background has not yet been established, and therefore one can drop the terms $T_{\rm L}$ and $y_{\rm L}$. T of eq.(13) is the gas kinetic temperature calculated in the last section, and $y_c = 1.1 \times 10^3 n f_{\rm HI} T^{0.73}$ (Scott & Rees, 1990).

Upon consideration of the self-absorption, the brightness temperature of the 21 cm radiation at redshift z is determined from the radiation transfer equation as

$$T_b(z) = T_{\rm CMB}(z) e^{-\tau(z)} + \int_0^{\tau(z)} T_s(z') e^{-\tau(z')} d\tau(z'), \tag{14}$$

where the first term on the right-hand side is from the CMB and the second term is from neutral hydrogen; $\tau(z)$ is the optical depth of the 21 cm absorption. When T_s is much larger than $T_* = h\nu_0/k_B = 0.06$ K, $\tau(z)$ is given by (Wild 1952, Field 1959)

$$\begin{aligned} \tau(z) &= \frac{3hc^3 A_{10} n f_{\rm HI}(z)}{32\pi\nu_0^2 k_B T_s(z) H(z)} \\ &\approx 2.7 \times 10^{-3} f_{\rm HI}(z) \left[\frac{T_{\rm CMB}(z)}{T_s(z)}\right] (1+z)^{1/2}, \end{aligned} \tag{15}$$

where we take the cosmological parameters $\Omega_m h^2 = 0.15$ and $\Omega_b h^2 = 0.02$. Since $\tau(z) \ll 1$, the observed brightness temperature excess at the redshifted frequency $\nu = \nu_0/(1+z)$ is

$$\begin{aligned} \delta T_b(\nu) &= [T_s(z) - T_{\rm CMB}(z)] \frac{1 - e^{-\tau(z)}}{1+z} \simeq \frac{T_s - T_{\rm CMB}}{1+z}\tau \\ &\simeq 7.3 \times 10^{-3} f_{\rm HI}(z) \left[\frac{T_s - T_{\rm CMB}}{T_s}\right] (1+z)^{1/2} \quad \text{K} \end{aligned} \tag{16}$$

3.2. Spatial Profiles of 21 cm Emission

In Figure 6, we show the profiles of the spin temperature $T_s(r)$ and 21 cm brightness temperature $\delta T_b(r)$ at time $t = 1,000$ for sources of $J_0 = 10^{-6}$, 10^{-4}, 10^{-2}, and 1, corresponding to $\dot{E} = 10^{39}$, 10^{41}, 10^{43} and 10^{45} ergs s^{-1}. Photons from the sources have power-law frequency spectrum with index $\alpha = 2$. The reionization redshift is taken to be $1 + z_r = 10$.

All sources exhibit 21 cm emission regions at $r > R_s$, where the gas is significantly heated, while the neutral hydrogen fraction is still high. Stronger sources generally have a larger and thicker region of 21 emission. The strongest source, $E_{\rm tot} = 10^{45}$ ergs s^{-1} shows a narrow region of the 21 cm emission. That is because for this strong source $t_i > 1000$, and therefore, the 21 cm emission region has not been formed yet. This picture can be clearly seen in comparisons between Figures 7 - 10, which show the formation of the 21 cm emission region for sources $E_{\rm tot} = 10^{39}$, 10^{41}, 10^{43} and 10^{45} ergs s^{-1}, respectively.

For a weak source, $E_{tot} = 10^{39}$ ergs s^{-1} as demonstrated in Figure 7, the profiles of $T_s(t, r)$ and $\delta T_b(t, r)$ are almost independent of t for $t > 200$. Obviously, as $t_i \ll 200$, there exists a stable structure of 21 cm emission region for this source, and Figure 7 shows the evolution of post-formation of the ionizing sphere.

Increasing the source intensity to $E_{\rm tot} = 10^{41}$ (Figure 8), the spatial profile of the 21cm emission does also show a stable structure when $t > 200$. But we can see a significant increase of the thickness of $\delta T_b(t, r)$ with time, because the t_i of this source is larger than that of $E_{tot} = 10^{39}$. Figure 8 displays also a post-t_i evolution.

In the case of $\dot{E} = 10^{43}$, we can see from Figure 3 that its t_i is in the range 200-400, and therefore, the profiles of $T_s(t, r)$ and $\delta T_b(t, r)$ (Figure 9) show a remarkable evolution from $t = 200$ to 1000. This gives the picture of the formation of 21 cm emission halo.

For the strongest source, $\dot{E} = 10^{45}$, Figure 3 shows its $t_i > 1000$. Therefore, Figure 10 is a pre-t_i evolution. Before the formation of a large and thick 21 cm emission halo, there is a very thin shell of 21 cm emission around the source. It will become thicker with the increase of the radial distance from the source.

From these numerical results, one can find that a 21 cm emission shell is typical for UV photon sources at the reionization epoch. The brightness temperature excess, δT_b of those 21 cm emission shells is about 20 mK. In the first stage of the shell formation, the radius of the shell increases with a velocity about the speed of light c. In later stage, the evolution of the shells become rather slow, and the radius and thickness of the shell are proportional to $\dot{E}^{1/3}$. For our case, the shell is approximately in the comoving range of (4 to 10) $\times$ $(\dot{E}/10^{45})^{1/3}$ Mpc.

3.3. Effect of Thermal Broadening

While including the thermal broadening, eq.(15) should be replaced by

$$\tau(z) = \frac{3hc^3 A_{10}}{32\pi\nu_0^2 k_B} \int_0^{z_r} \frac{n_{\rm HI}(z')}{T_s(z')H(z')} F(z,z')dz', \tag{17}$$

where the factor $F(z,z')$ is the normalized Dopper broadening line profile as

$$F(z,z') = \frac{1}{\sqrt{\pi}b(1+z)} e^{-\left(\frac{z'-z}{b(1+z)}\right)^2}, \tag{18}$$

with $b = (2k_BT/mc^2)^{1/2}$. For gas with temperature $\leq 10^4$ K, we have $b \simeq 5\times10^{-5}$, and the comoving scale is thus $D = 5\times10^{-5}(1+z)c/H(z)$. In the ΛCDM model at $(1+z)=10$, we have $D \simeq 0.10$ h^{-1} Mpc. Accordingly, the Doppler broadening will smooth out the 21 cm emission regions around sources with $\dot{E} \leq 10^{39}$ ergs s^{-1}. All sources with $\dot{E} \geq 10^{39}$ will survive under the Doppler broadening.

4. Discussions and Conclusions

We show that a common feature of UV sources in the reionization epoch is to form a 21 cm emission region. In the first stage the ionizing and heating fronts of IGM are coincident, and propagate with the speed of light. The evolution enters in the second stage, when the frequency spectrum of UV photons is hardened due to the loss of soft photons by reionization. In the hardened stage of the UV photon spectrum, the propagation speeds of both the ionizing and heating fronts are less than that of light, but the heating front is always moving faster than the ionizing front. In the spherical shell between the ionizing and heating fronts, the IGM is heated to $T \simeq 10^4$, while atoms are almost neural. The scales (radius and thickness) of the shell are approximately proportional to $\dot{E}^{1/3}$, if these scales are larger than the mean free path of ionizing photons at reionization.

The shell is the region of 21 cm emission. The brightness temperature excess upon the CMB is about 20 mK. For a strong source, like $\dot{E} = 10^{45}$ ergs s^{-1} and power-law spectrum ν^{-2} at $1+z=10$, the 21 cm emission shell is in the radial (comoving) range from 4 to 10 h^{-1} Mpc. Therefore, it would be detectable with radio observation in the band of 140 MHz, and with angular resolution equal to or better than a few arcmin, and spectral resolution equal to or better than 140 MHz $\times\ 10^{-3} = 0.14$ MHz. These conditions would be achieved with the planned and ongoing projects. This conclusion is still available for $\alpha \neq 2$.

In our calculation, the cosmic baryon gas is not described by the hydrodynamic equation, but treated only as a medium including effects of heating, cooling and ionization. This

treatment would be reasonable as hydrodynamic effects are generally significant on the spatial and temporal scales given by sound speed, which are quite different from the scales of the formation and evolution of the 21 cm emission regions. Therefore, most conclusions on the 21 cm emission patches will still survive even if the hydrodynamics of baryon gas is taken account of.

This work is supported in part by the US NSF under the grants AST-0506734 and AST-0507340. LLF acknowledges support from the National Science Foundation of China under the grant 10573036.

A. Equations of Radiative Transfer

For an ionized sphere associated with a point photon source, the radiation transfer (RT) equation is (Bernstein, 1988, Qiu et al. 2006)

$$\frac{\partial J}{\partial t}+\frac{1}{r^2}\frac{\partial}{\partial r}\left(r^2 n^r J\right)=-k_\nu J+S \tag{A1}$$

where $J(t,\mathbf{x},\nu,n_i)$ is the specific intensity, a the cosmic factor, $H=\dot{a}/a$, ν the frequency of photon and n_i a unit vector in the direction of photon propagation. In eq.(A1), we take $c=1$. k_ν and S are, respectively, the absorption and sources of photons. The absorption coefficient of eq.(1) is given by

$$k_\nu=\sigma(\nu)n_{\rm HI}(t,\mathbf{x}) \tag{A2}$$

where the cross section $\sigma(\nu)=6.3\times10^{-18}(\nu_0/\nu)^3$ cm^2.

The number density of neutral hydrogen H I, $n_{\rm HI}(t,\mathbf{x})$, is determined by

$$\frac{df_{\rm HI}}{dt}=\alpha_{\rm HII}n_e f_{\rm HII}-\Gamma_{\gamma\rm HI}f_{\rm HI}-\Gamma_{\rm eHI}n_e f_{\rm HI}, \tag{A3}$$

Relevant parameters are taken from Theuns et al. (1998) as

1. recombination coefficient

$$\alpha_{\rm HII}=6.30\times10^{-11}T^{-1/2}T_3^{-0.2}/(1+T_6^{0.7}), \tag{A4}$$

where T is temperature, and $T_n=T/10^n$.

2. collision ionization

$$\Gamma_{\rm eHI}=1.17\times10^{-10}T^{1/2}e^{-157809.1/T}(1+T_5^{1/2})^{-1} \tag{A5}$$

3. photoionization

$$\Gamma_{\gamma \rm HI}(t,r) = \int_{\nu_0}^{\infty} d\nu \frac{J(t,r,\nu)}{h\nu}\sigma(\nu). \tag{A6}$$

The temperature T is determined by the equation

$$k_{\rm B}\frac{dT}{dt} = H - C. \tag{A7}$$

4. heating rate.

$$H = \frac{1}{n} f_{\rm HI} \int_{\nu_0}^{\infty} d\nu J(t,r,\nu)\sigma(\nu)\frac{\nu-\nu_0}{\nu} \tag{A8}$$

where $h\nu_0 = 2.176 \times 10^{-11}$ ergs.

5. cooling. Since only the recombination cooling is important, we have

$$\begin{aligned} C &= 8.70 \times 10^{-27} T^{1/2} T_3^{-0.2} (1+T_6^{0.7})^{-1} [1-f_{\rm HI}]^2 \\ &+ 1.42 \times 10^{-27} T^{1/2} [1-f_{\rm HI}]^2 \\ &+ 2.45 \times 10^{-21} T^{1/2} e^{-157809.1/T} (1+T_5^{1/2})^{-1} (1-f_{\rm HI}) f_{\rm HI} \\ &+ 7.5 \times 10^{-19} e^{-118348/T} (1+T_5^{1/2})^{-1} (1-f_{\rm HI}) f_{\rm HI} \end{aligned} \tag{A9}$$

where $T_n = T/10^n$. The terms on the r.h.s. of eq.(16) are, respectively, the recombination cooling, collisional ionization cooling, collisional excitation cooling and bremsstrahlung. Both H and C are in the unit of ergs cm^3 s^{-1}.

B. Numerical Algorithm

In our numerical calculation, we solve the system of equations (6), (7) and (9) for the specific intensity J, the fraction of the neutral hydrogen f_{HI} and the temperature T as functions of the radius r, frequency ν and time t. In order to approximate the spatial derivative in (6), we adopt the fifth-order finite difference WENO scheme with anti-diffusive flux corrections. The fifth-order finite difference WENO scheme was designed in (Jiang & Shu 1996) and the anti-diffusive flux corrections to the high order finite difference scheme was designed in (Xu & Shu 2005). The objective of the anti-diffusive flux corrections is to sharpen the contact discontinuities in the numerical solution of the WENO scheme as well as to maintain high order accuracy. A fourth order quadrature formula is used in the computation of integration in equations (8) and (A8). Third order TVD Runge-Kutta time discretization is used in time integration for the system of equations (6), (7) and (9).

- The computational domain:
  The computational domain is $(r, \nu) \in [0, r_{max}] \times [1, \nu_{max}]$, where r_{max} and ν_{max} are chosen such that $J(r, \nu, t) \approx 0$ for $r > r_{max}$ or $\nu > \nu_{max}$. In our computation, $r_{max} = 1200$ and $\nu_{max} = 10^6$. The computational domain is discretized into a uniform mesh in the r-direction and into a smooth non-uniform mesh in the ν-direction. The uniform mesh in the r-direction is

$$r_i = i\Delta r \quad with \quad \Delta r = r_{max}/N_r, \quad i = 0, ..., N_r$$

  and the non-uniform mesh in the ν-direction is taken to be

$$\nu_j = 2^{\xi_j} \quad with \quad \xi_j = j\Delta\xi, \quad \Delta\xi = \log_2 \nu_{max}/N_\nu, \quad j = 0, ..., N_\nu$$

  which is allowed because only integration, e.g. in equations (8) and (A8), is involved in the computation with respect to the ν-variable. In our model, large ν contributes little in equations (8) and (A8), therefore the non-uniform mesh is designed in a way such that the mesh becomes coarser for larger ν.

- The spatial derivative in equation (6):
  WENO scheme with anti-diffusive flux corrections is used, which we refer to (Qiu et al. 2006) for details of implementation.

- The integration in equations (8) and (A8):
  We use a fourth order quadrature formula

$$\int_{\nu_0}^{\infty} f(x)dx = \Delta x \sum_{j=j_0}^{\infty} w_j f(j\Delta x) + O(\Delta x^4) \tag{B1}$$

  where $\nu_0 = j_0\Delta x$, and the weights w_j are given by

$$w_{j_0} = \frac{3}{8}, \quad w_{j_0+1} = \frac{7}{6}, \quad w_{j_0+2} = \frac{23}{24}, \quad w_{j_0+j} = 1, \qquad \text{for} \quad j > 2.$$

  Again we refer to (Qiu et al. 2006) for details of implementation.

- The time integration for the system of equations (6), (7) and (9).
  The third order TVD Runge-Kutta time discretization in (Shu & Osher 1988) for the system of ODEs $u_t = L(u)$ is

$$u^{(1)} = u^n + \Delta t L(u^n, t^n) \tag{B2}$$

$$u^{(2)} = \frac{3}{4}u^n + \frac{1}{4}(u^{(1)} + \Delta t L(u^{(1)})) \tag{B3}$$

$$u^{n+1} = \frac{1}{3}u^n + \frac{2}{3}(u^{(2)} + \Delta t L(u^{(2)})) \tag{B4}$$

The difficulty of a direct implementation of the scheme lies in the stiffness of equations (7) and (9). Especially for strong sources, when J(r=0) is large, one needs very small time step Δt to guarantee the stability of the numerical scheme, therefore huge computational cost for long time integration.

By observing that

- Though (7) and (9) are stiff ODEs, (6) involving the spatial derivative is not a stiff equation.
- The WENO procedure with the anti-diffusive flux corrections in approximating the spatial derivative is the major cost at each time step.
- Implicit numerical method in time evolution has milder time step restriction than the explicit one.

we have settled down with the following strategies to save the computational cost

- We use different time scales to solve J in (6) and to solve f_{HI} and T in (7) and (9). The time step for J, say Δt, is larger, while the time step for f_{HI} and T, say $\delta t = \frac{\Delta t}{N_t}$ with N_t being the number of small time steps in a large time step, is much smaller. By doing this, we take advantage of the non-stiffness of (6) and eliminate the cost of the WENO procedure with flux corrections for each small time step.
- In each small time step δt, we use a semi-implicit numerical method for strong sources to proceed in time for f_{HI} and T, which greatly releases the severe time step restriction for the sake of the stability of the scheme. The number of small time steps δt in one large time step Δt is thus greatly reduced, hence the saving of the computational cost.

More precisely, we modify the third order TVD Runge-Kutta time discretization in the following procedure

1. We have the initial condition of J, f_{HI} and T at t=0. Let us denote

$$J^0 = \left(J^0_{i,j}\right)_{N_r \times N_\nu} = \left(J(x_i, \nu_j, t=0)\right)_{N_r \times N_\nu},$$

$$f^0_{HI} = (f^0_{HIi})_{N_r \times 1} = \left(f^0_{HI}(x_i, t=0)\right)_{N_r \times 1}; \quad T^0 = (T_i)_{N_r \times 1} = \left(T(x_i, t=0)\right)_{N_r \times 1}.$$

2. For a large time step Δt, we evolve J^n, f^n_{HI} and T^n by three inner stages to J^{n+1}, f^{n+1}_{HI} and T^{n+1}.
   - J^{n+1}:
     $J^{(1)}$, $J^{(2)}$, J^{n+1} are updated according to (B2), (B3), (B4).

– f_{HI}^{n+1}, T^{n+1}:
Let us denote

$$\bar{h} = (h_1, h_2) = (f_{HI}, T)$$

and

$$\begin{aligned} \bar{L}(J, f_{HI}, T) &= (L_1(J, f_{HI}, T),\ L_2(J, f_{HI}, T)) \\ &= \left(\frac{1}{c\sigma_0}\{\ rhs\ of\ (7)\},\ \frac{1}{c\sigma_0 k_B}\{\ rhs\ of\ (9)\}\right) \end{aligned}$$

Instead of (B2), $f_{HI}^{(1)}$ and $T^{(1)}$ are evolved by

$$(f_{HI}^{(1)}, T^{(1)}) = \bar{h}_{(N_t)}$$

where $\bar{h}_{(N_t)}$ is the evolution of solution by the Euler-forward method for N_t times, with the Euler-forward method at each time step defined as

$$\bar{h}_{(j+1)} = \bar{h}_{(j)} + \delta t \bar{L}(J^n, \bar{h}_{(j)}); \tag{B5}$$

Instead of (B3), the second inner stage $\bar{h}^{(2)}$=$(f_{HI}^{(2)}, T^{(2)})$ is updated by

$$\bar{h}^{(2)} = \frac{3}{4}\bar{h}^n + \frac{1}{4}\bar{h}^{(2')}$$

with $\bar{h}^{(2')} = \bar{h}_{(N_t)}$ being the evolution of the solution by the Euler-forward method for N_t times based on $J^{(1)}$ as

$$\bar{h}_{(j+1)} = \bar{h}_{(j)} + \delta t \bar{L}(J^{(1)}, \bar{h}_{(j)}); \tag{B6}$$

Finally, instead of (B4), f_{HI}^{n+1} and T^{n+1} are computed as

$$\bar{h}^{n+1} = \frac{1}{3}\bar{h}^n + \frac{2}{3}\bar{h}^{(3')}$$

with $\bar{h}^{(3')} = \bar{h}_{(N_t)}$ obtained in a similar manner as in the previous step but based on $J^{(2)}$

$$\bar{h}_{(j+1)} = \bar{h}_{(j)} + \delta t \bar{L}(J^{(2)}, \bar{h}_{(j)}). \tag{B7}$$

3. When the source is strong, (7) and (9) suffer from severe time step restriction, we use a semi-implicit scheme instead of (B5) in our code to release the severe time step restriction and to save computational cost. The procedure of the implementation is the same as described above except that (B5) is replaced by

$$f_{HI(j+1)} = f_{HI(j)} + \delta t L_1(J^n, f_{HI(j+1)}, T_{(j)}) \tag{B8}$$

$$T_{(j+1)} = T_{(j)} + \delta t L_2(J^n, f_{HI(j+1)}, T_{(j+1)}) \tag{B9}$$

(B8) is computed by solving a quadratic equation with root located between 0 and 1, since L_1 is a quadratic function of f_{HI}, and (B9) is computed by the Newton iteration method. (B6) and (B7) are modified in the similar way as (B5).

- Boundary conditions:
  - Inflow boundary condition at r=0:
    $J_{i,j} = J_{0,j}, \qquad for \qquad i = 0, -1, -2.$
  - The boundary condition at $r = r_{max}$:
    $J_{N_r+i,j} = J_{N_r-1,j}, \qquad for \qquad i = 0, 1, 2$

REFERENCES

Bernstein, J., 1988, Kinetic Theory in the Expanding Universe, Cambridge

Cen, R. & Haiman, Z., 2000, ApJL, 542, L75

Feng, L.L., Shu, C.-W., & Zhang, M.P., 2004, ApJ, 612, 1

Field, G.B., 1958, Proc. IRE, 46, 240

Field, G.B., 1959, ApJ, 129, 536

He, P., Liu, J., Feng, L.-L., Bi, H.-G. & Fang, L.Z., 2004, ApJ, 614, 6

Jiang, G. & Shu, C.-W., 1996, J. Comp. Phys., 126, 202

Madau, P. & Rees, M., 2000, ApJL, 542, L69

Osterbrock, D., 1989, Astrophysics of Gaseous Nebulae and Active Galactic Nuclei, University Science Books, California

Page L. et al., 2006, astro-ph/0603449

Peterson, J., Pen, U.-L. & Wu, X.P., 2005, astro-ph/0502029

Qiu, J.-M., Shu, C.-W., Feng, L.-L. & Fang, L.Z., 2006, NewA, to appear.

Rottgering, H. 2003, NewA, 47, 405

Scott, D. & Rees, M. 1990, MNRAS, 247, 510

Shu, C.-W. & Osher, S., 1988, J. Comp. Phys., 77, 439

Spitzer, L., 1978, Physical Processes in the Interstellar Medium, John Wiley & Sons, NY

Strömgren, B., 1939, ApJ, 89, 529

Theuns, T., Leonard, A., Efstathiou, G., Pearce, F.R. & Thomas, P.A., 1998, MNRAS, 301, 478

Tozzi, P., Madau, P., Meiksin, A. & Rees, M. 2000, ApJ, 528, 597.

van de Weygaert, R. & van Albada, T.S., 1996, astro-ph/9602096

Wild, J.P., 1952, ApJ, 115, 206

Wyithe, S. & Loeb, A., 2004, ApJ, 610, 117

Xu, Z. & Shu, C.-W., 2005, J. Comp. Phys., 205, 458

Yu, Q.J., & Lu, Y.J., 2005, ApJ, 621, 31

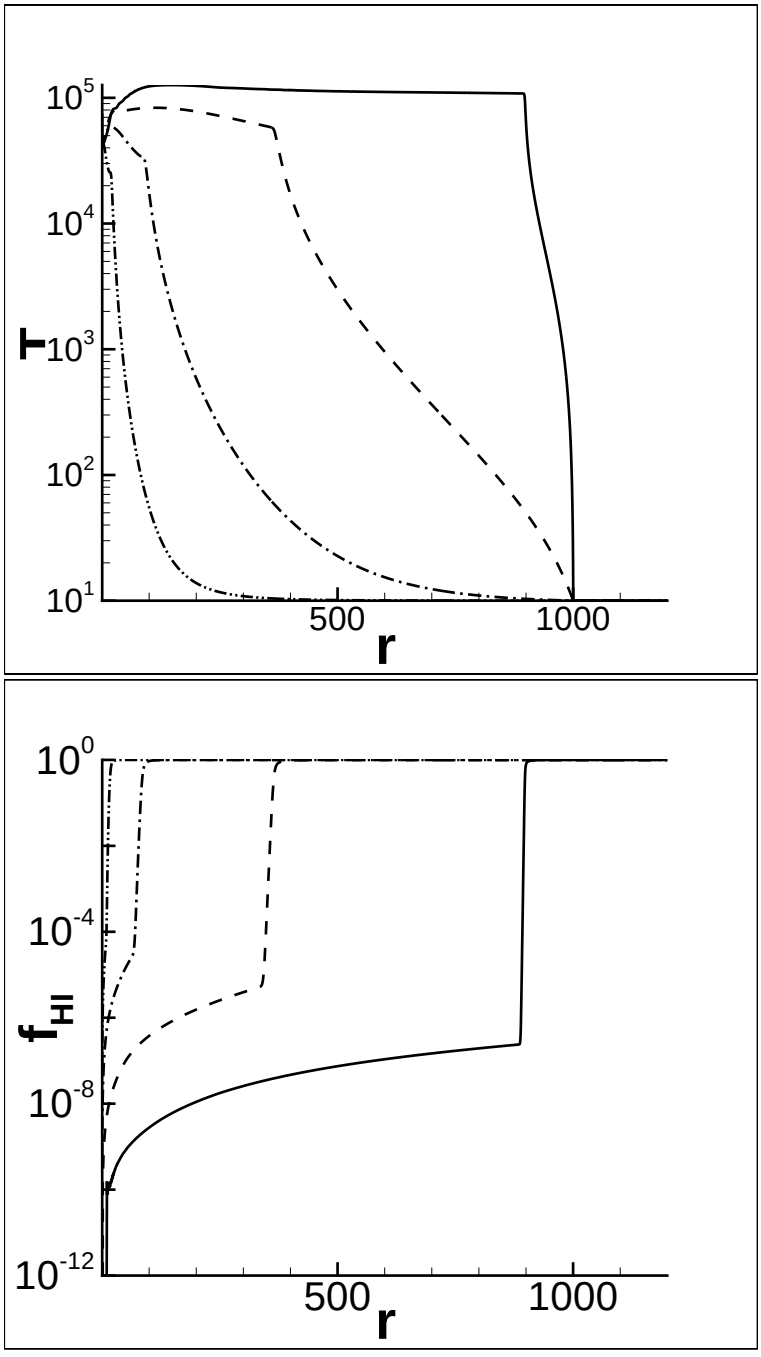

Fig. 1.— Profiles of $T(r)$ (top panel) and $f_{\rm HI}(r)$ (bottom panel) at time $t = 1,000$ for sources with intensity of $J_0 = 10^{-6}$ (dash dot dot), 10^{-4} (dash dot), 10^{-2} (dash), and 1 (solid), corresponding to $\dot{E} = 10^{39} - 10^{45}$ erg s^{-1} and power-law frequency spectrum with index $\alpha = 2$. The reionization redshift is taken to be $1 + z_r = 10$.

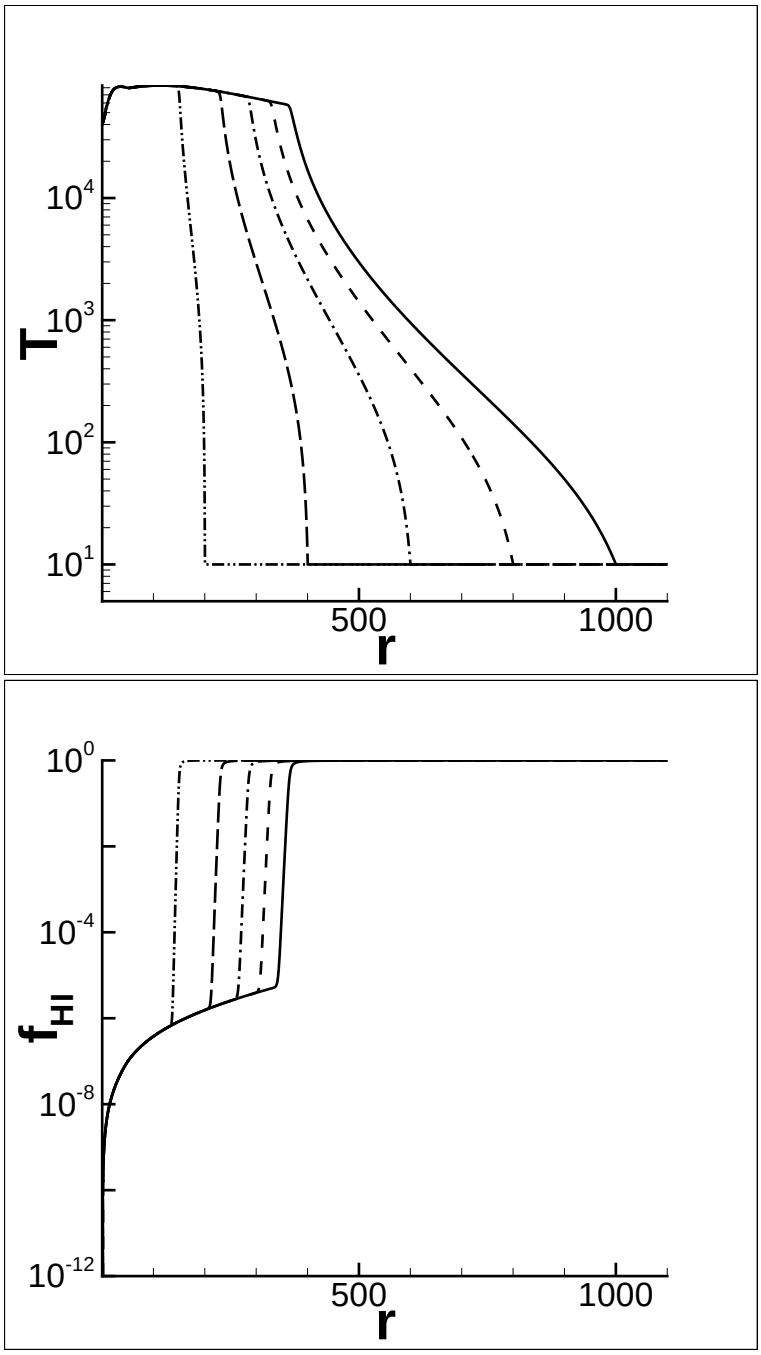

Fig. 2.— The profiles of $T(t, r)$ (top panel) and $f_{\rm HI}(t, r)$ (bottom panel) for a source of $J_0 = 10^{-2}$ at time $t = 200$ (dash dot dot), 400 (long dash), 600 (dash dot), 800 (dash), and 1,000 (solid line). Other parameters are the same as those in Figure 1.

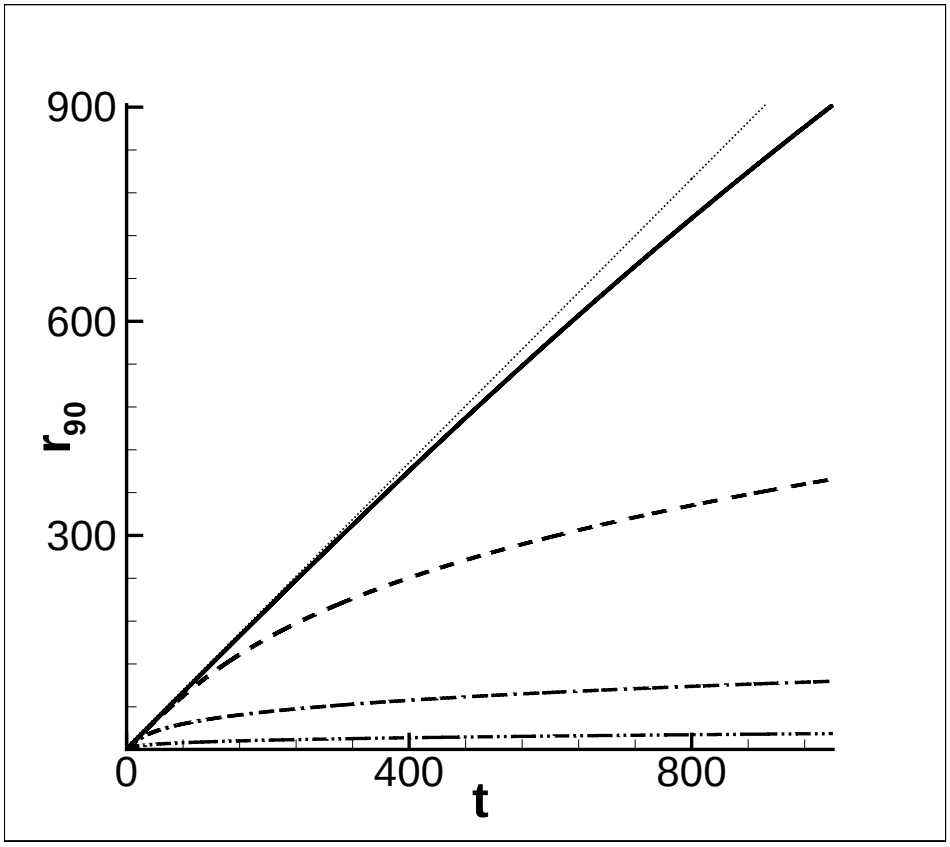

Fig. 3.— The evolution of $r_{90}(t)$, which is the solution of $f_{\rm HI}(t, r_{90}) = 0.90$. The sources are taken to be $J_0 = 10^{-6}$ (dash dot dot), 10^{-4} (dash dot), 10^{-2} (dash), and 1 (solid line), corresponding to $\dot{E} = 10^{39} - 10^{45}$ erg s^{-1}. Other parameters are the same as those in Figure 1. The dot line is $r_{90} = t$.

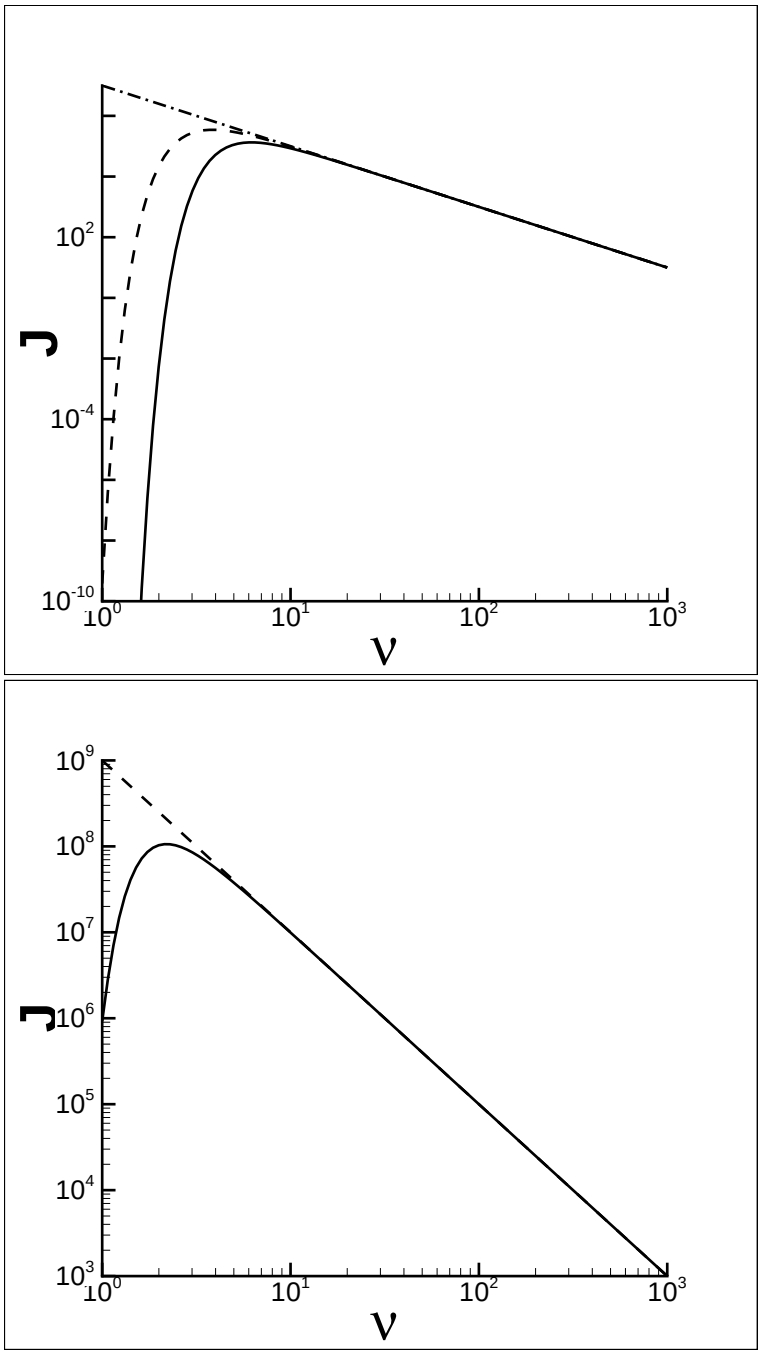

Fig. 4.— $J(t, r, \nu)$ vs. $\log \nu$ at time $t = 1,000$. 1.) Up panel: for the source $J_0 = 10^{-2}$ at $r = 300$ (dash dot), 400 (dash) and 500 (solid line); and 2.) Bottom panel: for the source $J_0 = 1$ at $r = 700$ (dash) and 900 (solid line).

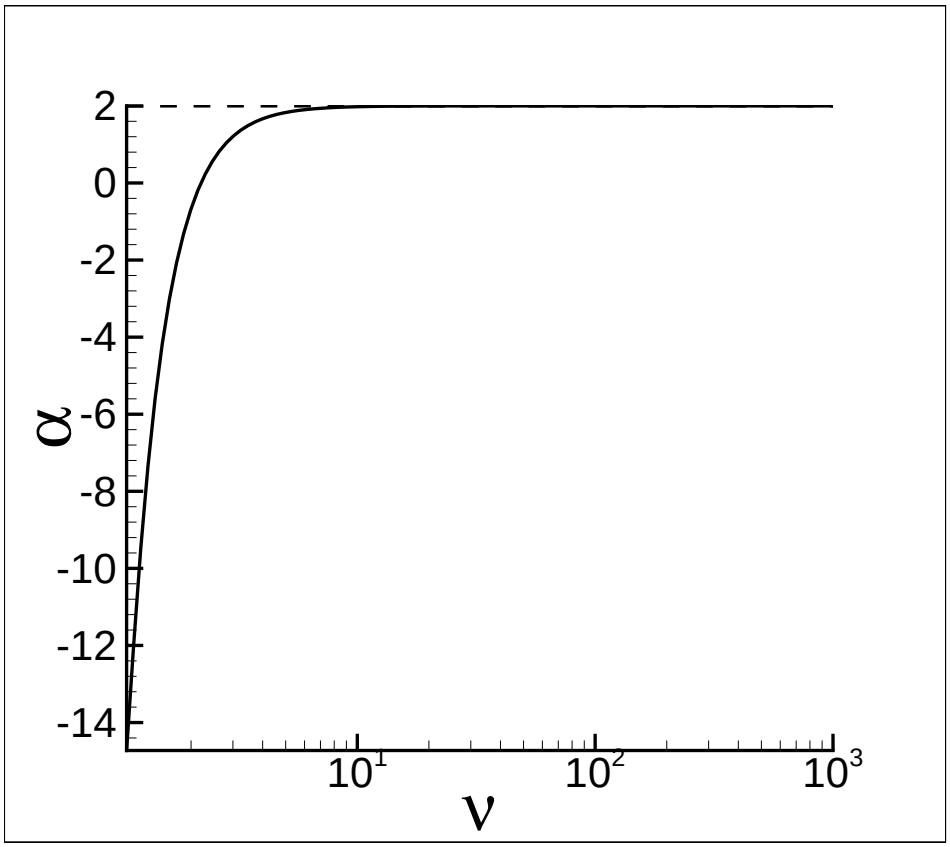

Fig. 5.— α vs. $\log\nu$ for the source $J_0 = 1$ at $r = 700$ (dash) and 900 (solid line).

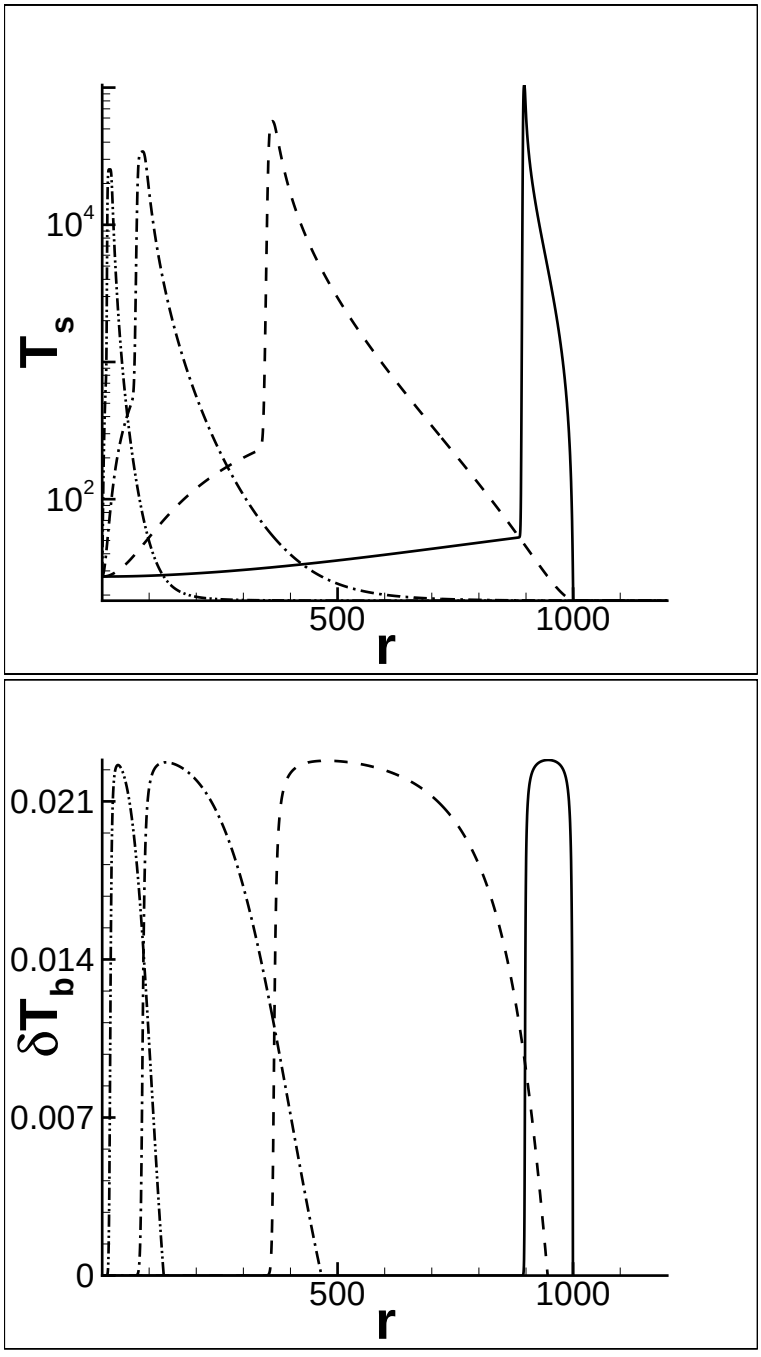

Fig. 6.— Profiles of $T_s(r)$ (top panel) and $\delta T_b(r)$ (bottom panel) at time $t = 1,000$ for sources with intensity of $J_0 = 10^{-6}$ (dash dot dot), 10^{-4} (dash dot), 10^{-2} (dash), and 1 (solid line), corresponding to $\dot{E} = 10^{39} - 10^{45}$ erg s^{-1} and power-law frequency spectrum with index $\alpha = 2$. The reionization redshift is taken to be $1 + z_r = 10$.

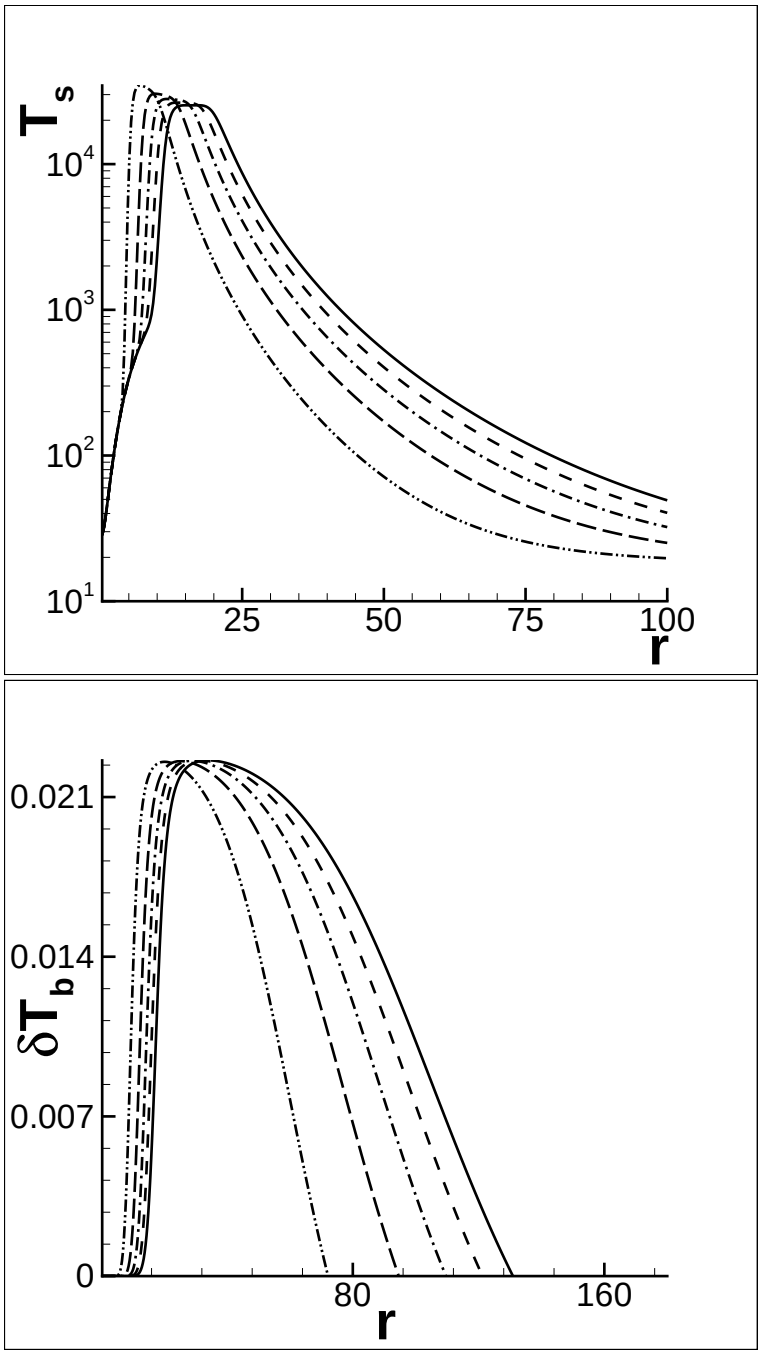

Fig. 7.— The profiles of $T_s(t,r)$ (top panel) and $\delta T_b(t,r)$ (bottom panel) for the source of $J_0 = 10^{-6}$ at time $t = 200$ (dash dot dot), 400 (long dash), 600 (dash dot), 800 (dash), and 1,000 (solid line). Other parameters are the same as those in Figure 6.

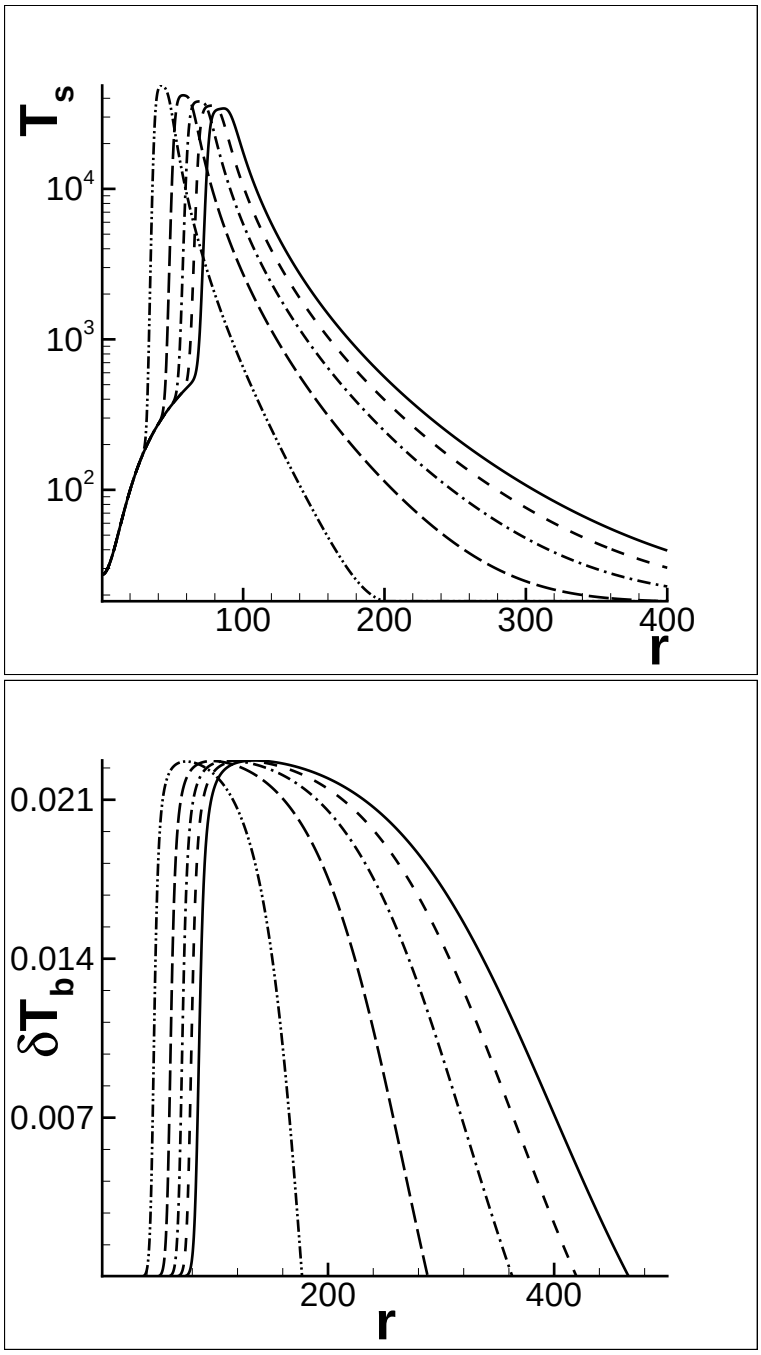

Fig. 8.— The profiles of $T_s(t,r)$ (top panel) and $\delta T_b(t,r)$ (bottom panel) for the source of $J_0 = 10^{-4}$ at time $t = 200$ (dash dot dot), 400 (long dash), 600 (dash dot), 800 (dash), and 1,000 (solid line). Other parameters are the same as those in Figure 6.

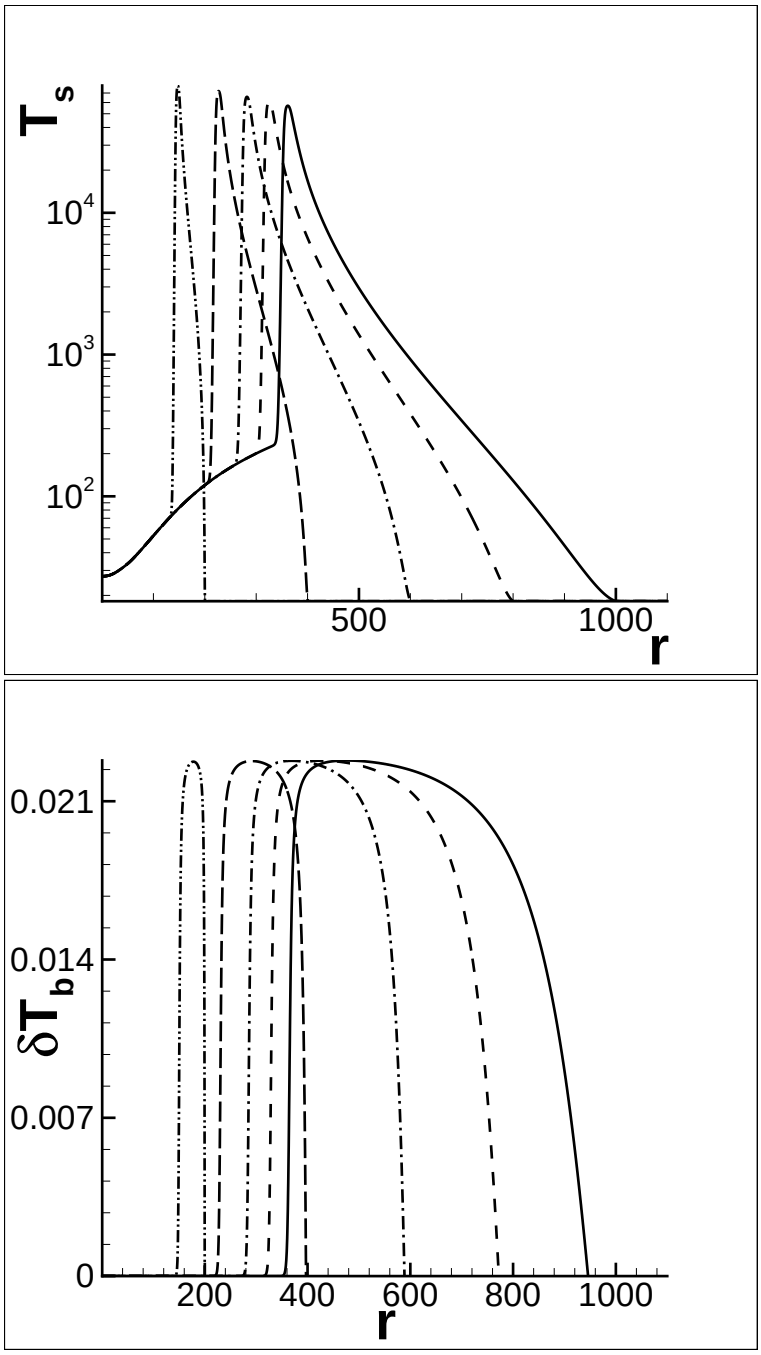

Fig. 9.— The profiles of $T_s(t,r)$ (top panel) and $\delta T_b(t,r)$ (bottom panel) for the source of $J_0 = 10^{-2}$ at time $t = 200$ (dash dot dot), 400 (long dash), 600 (dash dot), 800 (dash), and 1,000 (solid line). Other parameters are the same as those in Figure 6.

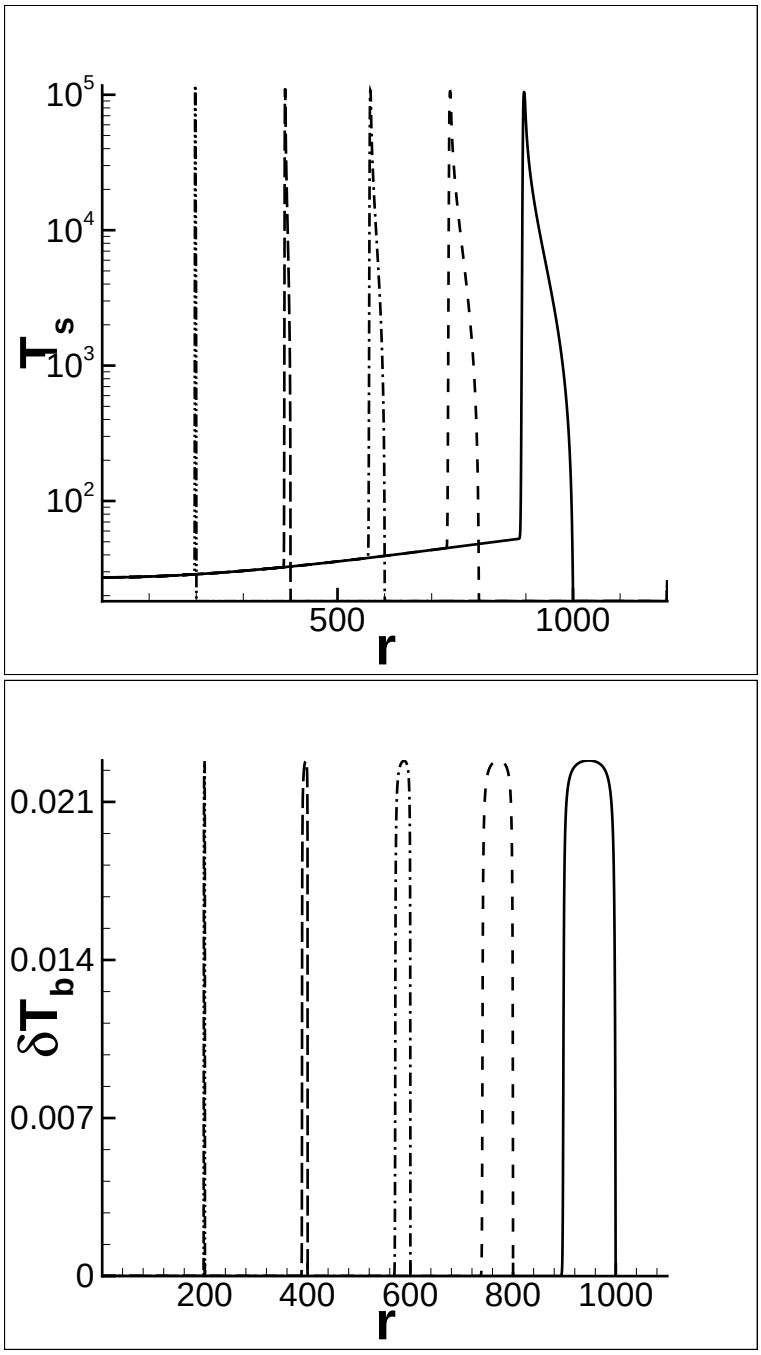

Fig. 10.— The profiles of $T_s(t, r)$ (top panel) and $\delta T_b(t, r)$ (bottom panel) for the source of $J_0 = 1$ at time $t = 200$ (dash dot dot), 400 (long dash), 600 (dash dot), 800 (dash), and 1,000 (solid line). Other parameters are the same as those in Figure 6.